Mechatronics 42 (2017) 52–68

Contents lists available at ScienceDirect

Mechatronics

journal homepage: www.elsevier.com/locate/mechatronics

The Flying Platform – A testbed for ducted fan actuation and control design☆

Michael Muehlebach*, Raffaello D'Andrea

Institute for Dynamic Systems and Control, Sonneggstrasse 3, 8092 Zurich, Switzerland

ARTICLE INFO

Article history:
Received 1 August 2016
Revised 21 October 2016
Accepted 7 January 2017

Keywords:
Unmanned aerial vehicle
Ducted fans
Thrust vectoring
System identification of an unmanned aerial vehicle
Control design of an unmanned aerial vehicle

ABSTRACT

This article discusses the design of an unmanned aerial vehicle whose purpose is to study the use of electric ducted fans as control and propulsion system. Thrust vectoring is essential for stabilizing the vehicle. We present measurement results characterizing the thrust vectoring capabilities of the propulsion system (both statically and dynamically), discuss a first-principle model describing the behavior of the flying machine, and analyze and quantify the controllability about hover. The first-principle model is subsequently used for a cascaded control design, which is shown to work reliably in practice. Furthermore, system identification results are discussed and used to extended the model. The resulting augmented model is shown to match the measured frequency response function.

1. Introduction

The design and control of unmanned aerial vehicles has been an active field of research in the past years, not least because of the numerous applications including surveillance, data acquisition, aerial photography, construction, transportation, and entertainment. Often, flying vehicles combining efficient forward flight, high maneuverability, and vertical take-off and landing capabilities are highly desirable. This article aims therefore at studying the properties of electric ducted fans as control and propulsion system for flying machines, where size is limited, but high static thrusts are required. This includes, for example, tailsitters, hovercrafts or even actuated wingsuit flight, [1].

To that extent, the Flying Platform, a flying vehicle actuated by three electric ducted fans is introduced, see Fig. 1.[1] In addition to their aerodynamic efficiency, [2, p. 322], resulting in high thrusts at moderate sizes, ducted fans have the advantage that the moving parts are shielded, protecting the propeller blades from undesired contacts with the environment. Moreover, the high exit velocities can be exploited for thrust vectoring. Thus, each ducted fan of the Flying Platform is augmented with an exit nozzle and control flaps to direct the airflow. The thrust vectoring is essential for stabilizing the vehicle.

The article includes experimental results characterizing the static maps from flap angles to thrusts, as well as the transfer functions from fan and servo commands to thrusts, thereby quantifying the available actuation bandwidth. For control and analysis purposes a low-complexity model is introduced. The mechanical design of the Flying Platform is optimized for maximum control authority; a closed-form expression for the determinant of the controllability Gramian is derived, providing a means to quantify and optimize the controllability of the vehicle by trading off the total inertia with the lever arm of the thrust vectoring system. The low-complexity model is used to derive a cascaded control law, stabilizing the vehicle about hover. The parameters of the control law are related to time constants of the closed-loop dynamics, which enables an intuitive tuning. The controller is shown to work reliably in flight experiments. A frequency domain system identification is presented, showing the limitations of the low-complexity model at frequencies below 1 Hz. We extend the model by including gyroscopic and aerodynamic effects, such as momentum drag (due to the redirection of the airflow by the ducted fans) yielding an augmented model that roughly matches the measured frequency response function.

Related work. Previous work, see e.g. [3–6], focused on aspects related to the modeling, the design and the control laws of flying vehicles with a single duct. The authors of [3] present a controller

☆ This paper was recommended for publication by Associate Editor Garrett M. Clayton.

* Corresponding author.
E-mail addresses: michaemu@ethz.ch (M. Muehlebach), rdandrea@ethz.ch (R. D'Andrea).

[1] A video showing the Flying Platform can be found under https://www.youtube.com/watch?v=NYY9q-vs4Nw.

http://dx.doi.org/10.1016/j.mechatronics.2017.01.001
0957-4158/

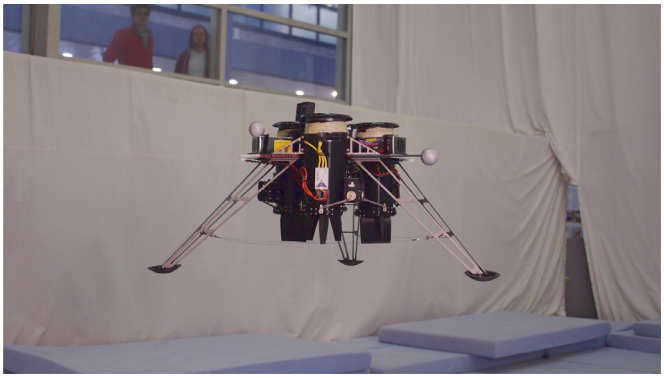

Fig. 1. The Flying Platform hovering in the Flying Machine Arena.

based on dynamic inversion of a low-complexity model in combination with a neural network for capturing the unmodeled dynamics. The control design is shown to work reliably in real world experiments. In [4], nonlinear control techniques are applied for simultaneous force and position tracking by a ducted-fan vehicle. The authors emphasize the unstable zero dynamics of the open-loop system, which is attributed to the fact that the thrust vectoring acts below the center of gravity, see also [7]. Other nonlinear control approaches include a sliding mode controller, [8], and nonlinear receding horizon control accounting for actuator saturations in [9]. In contrast, the authors in [10] present a linear cascaded control design and a linear estimator design for a ducted-fan vehicle with two counter-rotating rotors. The authors emphasize the benefits of the cascaded control design with regards to a practical implementation. In [5] and [6], the effects of crosswinds on the aerodynamics of a ducted fan vehicle are discussed. It is pointed out that the redirection of crosswinds by the propeller and the duct results in a drag force, linearly dependent on the forward velocity of the flying vehicle. This force induces a pitching moment on the center of gravity leading to an unstable open-loop system. This effect is further investigated in [11] by means of computational fluid dynamics and wind tunnel testing (see also [12] for further experimental results). The authors of [13] use a planar particle image velocimeter system to investigate the velocity profile in ducted fans. Both experimental data and computational predictions based on the Navier–Stokes equation are shown to agree at hover, as well as for horizontal movements. The results confirm that a horizontal movement redirects, respectively distorts the incoming airflow.

In [14] and [15], 4 ducted fans are assembled in a quadrotor configuration and the resulting flight performance is analyzed. Thereby two ducted fans are counter rotating for stabilizing yaw. In a more recent work, the authors of [16] compare and implement several extensions to a standard quadrotor configuration: 1) a quadrotor that can tilt its rotors, 2) a quadrotor that is extended with two ducted fans, both of which can vector the thrust, 3) four ducted fans aligned in a quadrotor configuration, all of which can vector the thrust. Thrust vectoring is achieved by moving the whole exit nozzle. The designs are motivated by the fact that these vehicles can perform position set point changes or compensate cross winds without requiring the vehicle to tilt. In all the designs, thrust vectoring is enhancing the maneuverability of the vehicle, but is not crucial for stability.

Compared to the ducted fan vehicles presented in the literature, the Flying Platform is significantly different. Instead of a relatively large shroud, covering a single or two counter-rotating propellers with rotary speeds of roughly 10, 000 rpm, see e.g. [3], three electric ducted fans, each of which can vector the thrust, are used to actuate the Flying Platform. Thurst vectoring is essential for stabilizing the vehicle. The electric ducted fans have a diameter of 90 mm, which is small compared to the overall dimension of the Flying Platform (about 1 m). Nevertheless, they provide a total thrust of roughly 45 N each, at around 30000 rpm, and achieve exit velocities up to 90 m/s.[2] The high exit velocities enable efficient thrust vectoring; compared to the single-duct vehicle presented in [3],[3] the thrust generated by the control surfaces of the Flying Platform is roughly 5–10 times larger. Moreover, the high rotation speeds of the ducted fans lead to gyroscopic torques, which are quantified by analyzing real flight data.

The characterization and modeling of flying vehicles with system identification techniques has a long history, [17]. In the past years, various models for different types of unmanned aerial vehicles have been identified. Helicopters are for example considered in [18], a fixed-wing aircraft in [19], and multirotors in [20]. A survey and categorization of these identification results can be found in [21]. We will present a non-parametric frequency domain-based system identification of the Flying Platform, which provides a means to asses the accuracy of two first-principle models with various degrees of complexity.

Outline. The hardware design is covered in Section 2, where the properties of a single actuation unit, comprising an electric ducted fan, an exit nozzle, and control flaps for thrust vectoring, are investigated. Both static and dynamic thrust measurements are presented. The section concludes by discussing how the actuation units are combined in the Flying Platform design. In Section 3, a low-complexity model describing the dynamics of the Flying Platform is presented. The dynamic model is used for optimizing the control authority of the thrust vectoring by the mechanical design, leading to a systematic trade-off between the lever arm and the total inertia of the vehicle. The model is also used for a cascaded control design as presented in Section 4. Flight tests show the effectiveness of the proposed control design. Section 5 discusses the results of a frequency domain system identification. It is shown that the low-complexity model explains the frequencies above 1 Hz well, but has limited predictive power at lower frequencies. It is argued that the model mismatch is possibly due to unmodelled aerodynamic effects, which are inherent to the ducted fan actuation. Therefore an augmented model is derived providing a better explanation of the measured data. The article concludes with final remarks in Section 6.

2. Hardware design

This section describes the hardware design of the Flying Platform. We start by presenting the design of a single actuation unit, before explaining how these are combined to actuate the Flying Platform.

2.1. Actuation unit

An actuation unit consists of an electric ducted fan, an outlet nozzle, and two control flaps for thrust vectoring, see Fig. 2.

The thrust is generated by the Schübeler DS-51-DIA HST electric ducted fan driven by the brushless DC motor DSM4640-950. According to the datasheet of the manufacturer the ducted fan is optimized for high static thrust, yielding exit velocities up to 90 m/s. This makes thrust vectoring particularly interesting, since the force resulting from a redirection of the airflow is proportional to the square of the airflow velocity. The electric ducted fan is embedded in a convergent exit nozzle, which has an inlet area of 6940 mm^2

[2] These values are taken from the datasheet of the fans.

[3] Other previously presented vehicles seem to be similar; [4]–[6] do not provide measurement results explicitly quantifying the thrust vectoring.

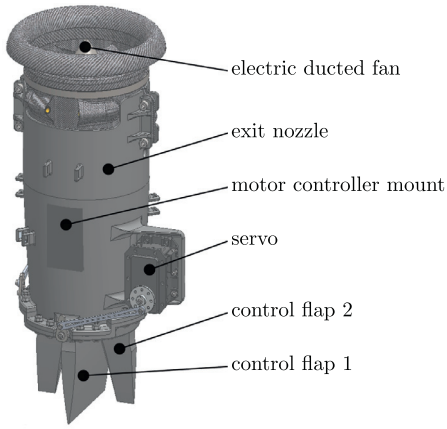

Fig. 2. The different components of a single actuation unit.

Fig. 3. Side and top view of control flap 2. The flap has 80 mm length (chord length) and 83 mm width. Compared to the control flap 1, which has the same dimensions and the same airfoil (NACA0015), a triangular part of control flap 2 is cut out.

and an outlet area of 5540 mm^2. Thus, the cross section is reduced by around 20% causing the airflow to accelerate through the nozzle. The motor controller (YGE 90HV) is mounted to the exit nozzle and is cooled by the airflow. More precisely, the fins that are attached to the motor controller are inserted in the airflow through the hole in the exit nozzle, as shown in Fig. 2. The hole in the exit nozzle is designed such that the motor controller holds in place (press fit). In addition, the outlet nozzle has a mount for the two servos (Dynamixel RX-24F), where each servo actuates a control flap. Both the outlet nozzle and the control flaps are 3D-printed in ABS-M30. The roughness average characterizing the surface roughness of the flaps and the exit nozzle is estimated to be around $R_a = 3.2$ µm. In [22], the impact of roughness on the lift characteristics of a NACA0015 airfoil is characterized. It is found that at a Reynolds number of 220,000, which is comparable to our setup, an increased roughness would reduce the produced lift up to 40%. However, an increased roughness also delays the airfoil's stall to higher angles of attacks (up to a factor of two). In our case, the flaps, which have likewise a NACA0015 profile, operate at relatively high angles of attack, and therefore the roughness of the airfoil is not necessarily a disadvantage, as it might prevent stall. Note that the effect of roughness seems strongly influenced by the Reynolds number and the specific airfoil. For example, the reduction of lift due to roughness reported in [23], where windtunnel tests with the DU300-mod airfoil at Reynolds numbers above 3.6×10^6 are presented, are less drastic.

The two control flaps are aligned orthogonally to simplify the mechanical design of the actuation mechanism. To achieve an actuation radius of $\pm$ 18° for both flaps, a triangular part of control flap 2 is cut out, thereby reducing the maximum thrust deviation achieved by control flap 2 approximately by a factor of two. A chord length of 80 mm is chosen for both flaps. The choice of the airfoil (NACA0015) is based on an optimization of the stall angle with the XFoil software package[4] at a Reynolds number of 350,000, corresponding to a typical airflow velocity of 70 m/s.[5]

Characterization of a single actuation unit. The available thrust, and the ability of the control flaps to vector thrust is characterized using force measurements with the transducer ATI Mini-40 using the SI-20-1 calibration. This results in a sensing range of $\pm$ 60 N in the vertical direction and $\pm$ 20 N in the horizontal direction, with a resolution of 0.01 N. The experimental results are presented in the following.

Static thrust measurements are shown in Fig. 4. A single actuation unit is attached to the load cell. The motorcontroller, the servos, and the load cell are interfaced using the PX4 flight management unit, [24]. The fan is run at a constant pulse-width modulation (PWM) rate, resulting in a constant thrust of 26.4 N when both control flaps point straight down (this corresponds roughly to the hover condition of the Flying Platform). Measurements are taken at 7 different flap angles, which is found to be enough for guaranteeing that the 68% confidence interval of a resulting linear fit is below 0.024 N/° (slope) and 0.27 N (offset). The flap angle is set by the servo, which has a resolution of 0.29°. For each flap angle, 500 measurement points are taken at a sampling frequency of 50 Hz. The standard deviation obtained at each measurement point is indicated by the bars shown in Fig. 4. The thrust measurements display a relatively large standard deviation, which is possibly due to the turbulent flow in the exit nozzle induced by the high Reynolds number, the roughness of the 3D print, and the motor controller mount, but also due to a slight play in the connection of the control flaps with the servos. Summarizing, a maximum horizontal thrust of 3 N can be generated by control flap 1, whereas control flap 2 generates a maximum horizontal thrust of 1.5 N. This is not unexpected, since compared to control flap 1, control flap 2 has roughly half the area available for deviating the thrust. Moreover, if control flap is fully inclined, the total thrust magnitude is reduced by around 2 N, as shown in Fig. 4 (bottom). The decrease in total thrust is not entirely symmetric. This might be caused by the motor controller mount that destroys the symmetry of the airflow through the exit nozzle.

Similar experiments are carried out for characterizing the total thrust as a function of the PWM rate given to the motorcontroller, see Fig. 5. The plateau that is visible above a duty cycle of 0.8 is most likely due to limitations of the motor controller. The rotational speed of the ducted fan is found to be roughly constant at a fixed PWM rate, as can be inferred from current measurements of a single motor phase. A linear fit through the data points neighboring the PWM rate of 0.6 is performed, and will be used later. The 68% confidence interval of the fit is 0.127 N/% for the linear part and 0.7 N for the offset.

Dynamic measurements reveal that the flap angle to thrust maps can be approximated by second-order systems, with a natural frequency of around 80 rad/s and a damping of roughly 0.4.

[4] See http://web.mit.edu/drela/Public/web/xfoil/.

[5] The airflow velocity estimate is based on momentum theory, [2, p. 322, equation (6.41)]. For the calculation of the Reynolds number a temperature of 30° C is assumed, which is motivated by the heat loss of the motor controller and the electrical motor. The parameter Ncrit that describes the transition criterion in XFoil is set to 7.

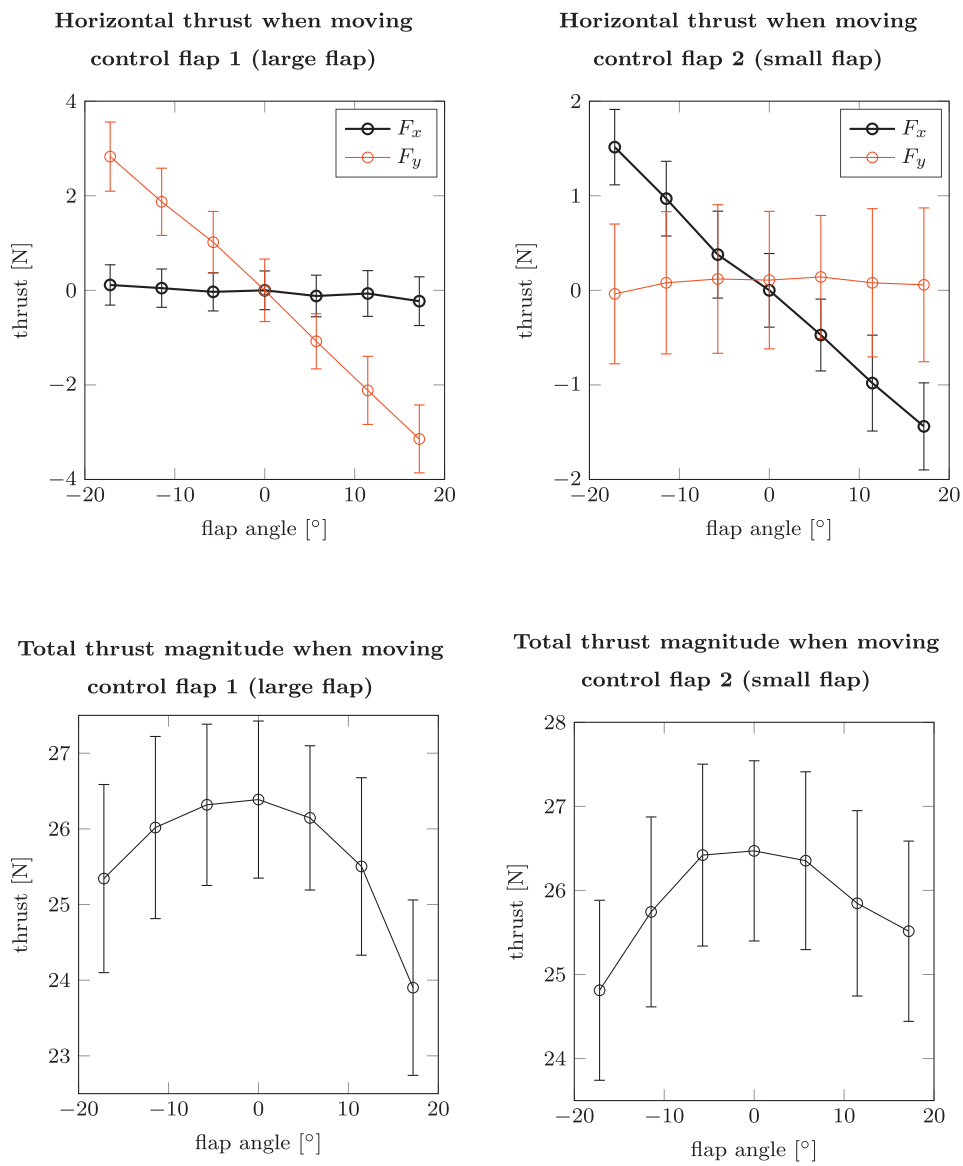

Fig. 4. Shown are the x and y-components of the thrust (top row) and the total thrust magnitude (bottom row), when moving control flap 1 (left row), respectively control flap 2 (right row). The x-axis is aligned with control flap 1, the y-axis with control flap 2.

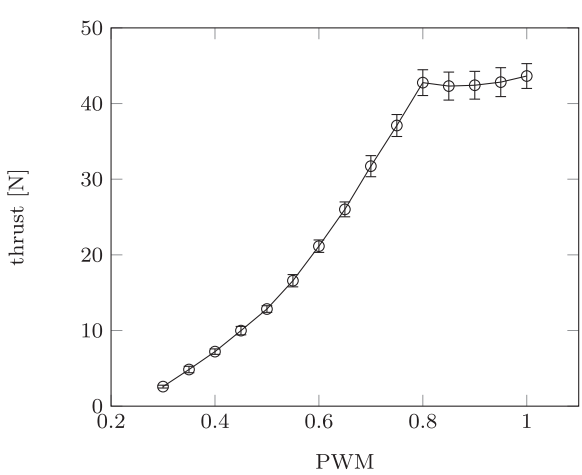

Fig. 5. Total thrust generated by the actuation unit (in the vertical direction), with both control flaps pointing straight down.

The map from PWM rate to total thrust (in case the control flaps are pointing straight down) behaves as a first-order system with a time constant of 0.01 s. The dynamic measurements were carried out using a similar procedure as presented in Section 5. The control flaps and the ducted fan are excited using multisine signals containing a flat frequency spectrum up to 20 Hz, respectively 10 Hz. The excitation signals have an amplitude below 10° for the flaps and an amplitude below 0.05 for the PWM rate controlling the fan. The sampling frequency is set to 100 Hz for the horizontal thrusts and 50 Hz for the vertical thrust, which is due to the limited update rate of the motor controller. The transfer function estimates are based on data collected over 62 periods, where the first two periods are discarded for eliminating transients. The experimental results are shown in Fig. 6 (control flap 1, control flap 2 is similar) and Fig. 7 (total thrust). The sharp resonance peak at 100 rad/s visible in Fig. 6 is attributed to the measurement setup. More precisely, it corresponds to the first eigenmode of the beam holding the load cell and the actuation unit. The parametric fit is obtained by minimizing a weighted residual, similar to Section 5.

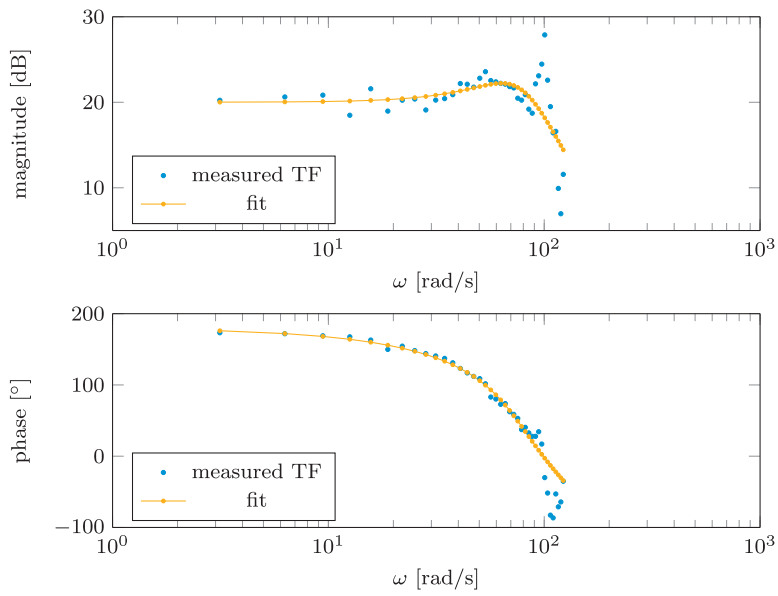

Fig. 6. Transfer function from the flap angle to the horizontal thrust.

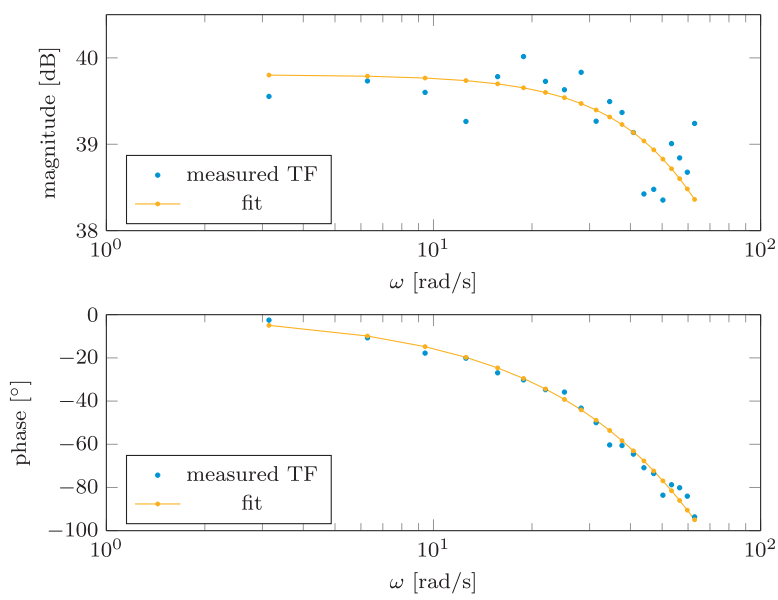

Fig. 7. Transfer function from the PWM rate to the vertical thrust.

2.2. Flying Platform

The Flying Platform design combines three actuation units, which are aligned with the corners of an equilateral triangle of 20 cm side length, as shown in Fig. 8. The actuation units are oriented such that the axis of the larger flap points to the center of the equilateral triangle. The fan units are mounted on a honeycomb carbon fibre sandwich structure. Three legs support the weight of the Flying Platform when it is on the ground. The electronics are located close to the estimated center of gravity. Table B.3 in Appendix B summarizes the mechanical specification of the Flying Platform.

The PX4 flight management unit, [24] is used to run the control algorithms. The motor controllers of the electric ducted fans are interfaced via PWM. Servo commands for actuating the control flaps are sent to the servos via a serial RS485 bus. Power is delivered by three 4-cell Thunderpower Magma batteries with 6600 mAh each. The power consumption at hover is around 6kW resulting

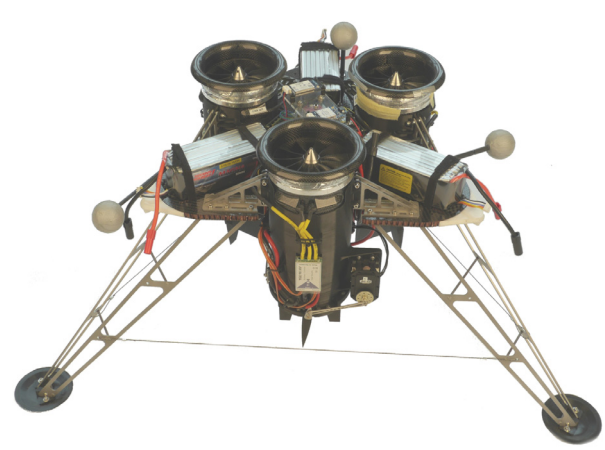

Fig. 8. The Flying Platform.

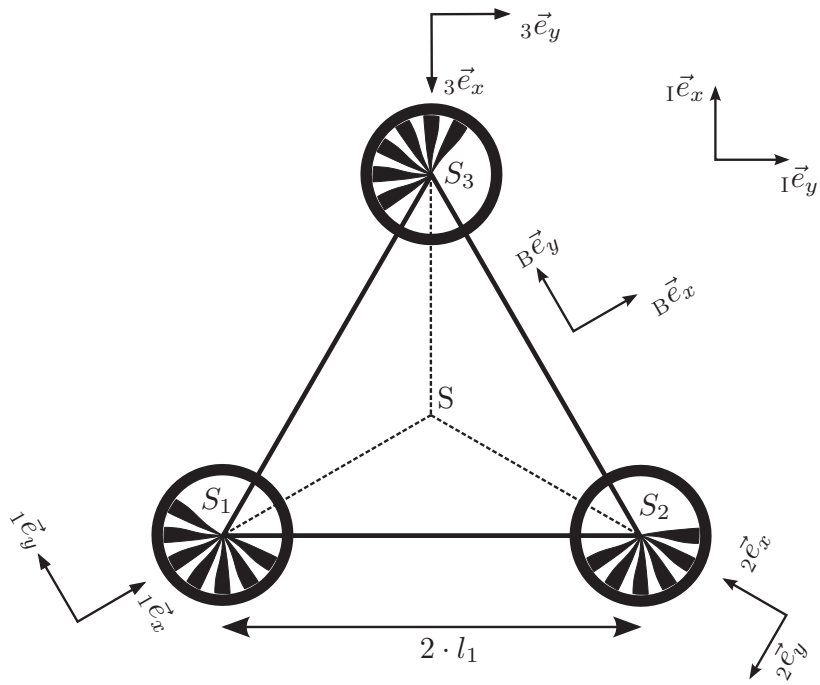

Fig. 9. Schematic outline of the Flying Platform showing the coordinate frames $\{I\}$, $\{i\}$, $i = 1, 2, 3$, and $\{B\}$ (courtesy of Tobias Meier).

in a flight time of around 3 min. The batteries weigh 680 g each, leading to a total weight of the Flying Platform of 8.0 kg.

3. Dynamics

This section presents a low-complexity model of the Flying Platform. The nonlinear equations of motion are linearized about hover for control and analysis purposes. We will optimize the determinant of the controllability Gramian as a function of the actuator placements and thereby maximize the controllability about hover.

Notation. We introduce an inertial coordinate system {I}, a body-fixed coordinate system {B}, and local body-fixed coordinate systems $\{i\}$ oriented along the control flaps of the actuation units, see Fig. 9. The projection of a tensor onto a particular coordinate frame is denoted by a preceding superscript, i.e. ${}^{\mathrm{B}}\Theta \in \mathbb{R}^{3\times 3}$, ${}^{\mathrm{B}}F \in \mathbb{R}^3$. The arrow notation, e.g. in Fig. 9, is used to emphasize that a vector (and tensor) should be a priori thought of as a linear object in a normed vector space detached from its coordinate representation in a particular coordinate frame. The transformation matrix $R_{\mathrm{IB}} \in \mathrm{SO}(3)$ relates vectors from the body-fixed frame to their representation in the inertial frame, that is ${}^{\mathrm{I}}v = R_{\mathrm{IB}}{}^{\mathrm{B}}v$, for all vectors ${}^{\mathrm{B}}v \in \mathbb{R}^3$. Moreover, the skew symmetric matrix corresponding to a vector $a \in \mathbb{R}^3$, denoted by $\tilde{a}$, is defined as $a \times b = \tilde{a}b$, for all $b \in \mathbb{R}^3$, where $a \times b$ refers to the cross product of the two vectors a and b. Since the body-fixed coordinate frame {B} is the most commonly projected coordinate frame, its preceding superscript is usually removed for ease of notation, that is, ${}^{\mathrm{B}}m = m$, ${}^{\mathrm{B}}\Theta = \Theta$, etc. The standard unit vectors in $\mathbb{R}^3$ are denoted by e_x, e_y, and e_z. Vectors are expressed as n-tuples $(x_1, x_2, \ldots, x_n)$ with dimension and stacking clear from the context.

Dynamics. The equations of motion can be derived, for example, by using the principle of virtual power, [25, Ch. 3]. To that extent, the moving parts of the ith actuation unit (turbine blades and shaft of the electrical motor) are separated from the remaining structure by introducing the constraint forces $\vec{\Lambda}_i$ and the motor torques $\vec{M}_{Ti}$, see Fig. 10. Requiring the virtual power to vanish for all virtual velocities (translational and rotational) yields the following characterization of the dynamic equilibrium,

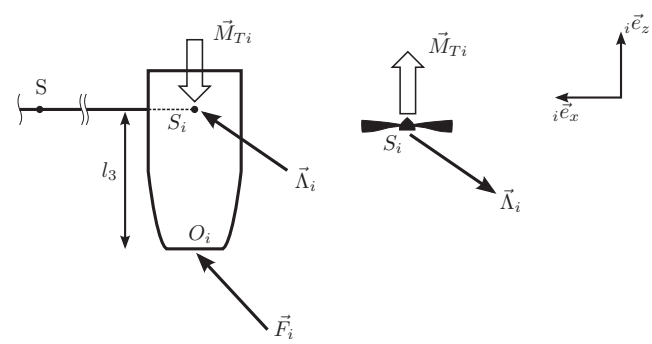

Fig. 10. Free body diagram of a single actuation unit (courtesy of Tobias Meier). The motor torque $\vec{M}_{Ti}$ is aligned with the z-axis of the local coordinate frame $\{i\}$. The vertical thrust, as well as the horizontal thrust generated by the two the control flaps are combined in the force $\vec{F}_i$.

$$\Theta\dot{\omega} + \sum_{i=1}^{3}\Theta_i\dot{\omega}_i = -\tilde{\omega}\left(\Theta\omega + \sum_{i=1}^{3}\Theta_i\omega_i\right) + \sum_{i=1}^{3}\tilde{r}_iF_i, \tag{1}$$

$$m{}^{\mathrm{I}}\dot{v} = m{}^{\mathrm{I}}g + \sum_{i=1}^{3}R_{\mathrm{IB}}F_i, \tag{2}$$

$$Ce_z^{\mathrm{T}}(\dot{\omega} + \dot{\omega}_i) = M_i, \quad i = 1, 2, 3, \tag{3}$$

where Θ denotes the total inertia of the Flying Platform referred to its center of gravity S, Θ_i the inertia of the moving parts of the ith ducted fan referred to its center of rotation, and m the total mass. The velocity of the center of mass of the vehicle is denoted by v, whereas ω refers to its angular velocity, i.e. the angular velocity of the frame $\{B\}$ with respect to frame $\{I\}$. The thrust generated by the ith actuation unit, that is, the vertical thrust from the electric ducted fan, vectored by the two control flaps, is denoted by F_i. The vector from the center of gravity to the point of origin of the force

F_i is denoted by r_i. Aerodynamic effects except the forces generated by the control flaps and the thrust of the fans are neglected. These will be included in an augmented model as presented in Section 5. The scalar M_i and the vector ω_i denote the torque of the electrical motor, respectively the angular rate (relative to the body-fixed frame $\{B\}$) of the ith ducted fan. The rotating parts (turbine blades and electrical motor) of the actuation units are assumed to be symmetric and rotate about their respective center of gravity resulting in[6]

$$\Theta_i =: \operatorname{diag}(\bar{C}, \bar{C}, C). \tag{4}$$

The angular velocity vector ω_i is assumed to have only a component along the z-axis of the body-fixed frame. Therefore its rate of change $\dot{\omega}_i$ appearing in (1) can be eliminated with (3) resulting in

$$\hat{\Theta}\dot{\omega} = -\tilde{\omega}\left(\Theta\omega + \sum_{i=1}^{3}\Theta_i\omega_i\right) + \sum_{i=1}^{3}(\tilde{r}_i F_i - e_z M_i), \tag{5}$$

where

$$\hat{\Theta} := \Theta - 3\, C e_z e_z^{\mathrm{T}}. \tag{6}$$

We will consider the thrusts generated by the actuation units and expressed in their local coordinate frames $\{i\}$ to be the inputs to the system. The servo and PWM-commands for the electric ducted fans are then calculated by inverting the linearization of the static maps presented in Section 2.1. The total thrust and the resulting torque are linear in the thrusts generated by the actuation units (the inputs), more precisely,

$$\sum_{i=1}^{3} F_i = T_1 u, \quad \sum_{i=3}^{3} \tilde{r}_i F_i = T_2 u, \tag{7}$$

where $u := ({}^1F_1, {}^2F_2, {}^3F_3)$,

$$T_1 := \begin{pmatrix} T_{11} \\ T_{12} \end{pmatrix}, \quad T_2 := \begin{pmatrix} T_{21} \\ T_{22} \end{pmatrix}, \tag{8}$$

with

$$T_{11} := \begin{pmatrix} 1 & 0 & 0 & -1/2 & -\sqrt{3}/2 & 0 & -1/2 & \sqrt{3}/2 & 0 \\ 0 & 1 & 0 & \sqrt{3}/2 & -1/2 & 0 & -\sqrt{3}/2 & -1/2 & 0 \end{pmatrix}, \tag{9}$$

$$T_{12} := \begin{pmatrix} 0 & 0 & 1 & 0 & 0 & 1 & 0 & 0 & 1 \end{pmatrix}, \tag{10}$$

$$T_{21} := l_3 J T_{11} + 2\sqrt{3}/3 l_1 V_1, \tag{11}$$

$$T_{22} := -2\sqrt{3}/3 l_1 \begin{pmatrix} 0 & 1 & 0 & 0 & 1 & 0 & 0 & 1 & 0 \end{pmatrix}, \tag{12}$$

$$V_1 := \begin{pmatrix} 0 & 0 & 0 & 0 & 0 & -\sqrt{3}/2 & 0 & 0 & \sqrt{3}/2 \\ 0 & 0 & 1 & 0 & 0 & -1/2 & 0 & 0 & -1/2 \end{pmatrix}, \tag{13}$$

$$J := \begin{pmatrix} 0 & 1 \\ -1 & 0 \end{pmatrix}. \tag{14}$$

As a result, the evolution of the center of gravity and the evolution of the angular velocity are given by

$$m^{\mathrm{I}}\dot{v} = m^{\mathrm{I}}g + R_{\mathrm{IB}} T_1 u, \tag{15}$$

$$\hat{\Theta}\dot{\omega} = -\tilde{\omega}\left(\Theta\omega + \sum_{i=1}^{3}\Theta_i\omega_i\right) + T_2 u - e_z \sum_{i=1}^{3} M_i. \tag{16}$$

[6] In fact, the expression remains unchanged if the inertia is expressed in the local frame $\{i\}$ or in a frame attached to the moving parts of fan i (as long as the z-axes are aligned).

Linearization. For control and analysis purposes the dynamics are linearized about hover. The three ducted fans are assumed to be identical and to rotate in the same direction. Thus, at hover, the torques M_i have the same values, that is, $M_i = M,\ i = 1, 2, 3$. Moreover, the torques M and the weight of the vehicle must be balanced by the thrust generated by the ducted fans and deviated by the control flaps, which is achieved by the thrust command

$$\begin{aligned} \bar{u} := (&0, -M\sqrt{3}/(2l_1), mg_0/3, \\ &0, -M\sqrt{3}/(2l_1), mg_0/3, \\ &0, -M\sqrt{3}/(2l_1), mg_0/3), \end{aligned}$$

where $g_0 := 9.81\ \mathrm{m/s^2}$ denotes the gravitational acceleration. For better readability the components of the vector $\bar{u}$ in the above equation are grouped according to the different actuation units, that is, the first line contains the x, y, and z-components of the thrust assigned to the first fan unit, the second line contains the thrust assigned to the second fan unit, etc. We further introduce Euler angles (α, β, γ) (roll, pitch, yaw) to parametrize the rotation matrix R_{IB}. Using the matrix exponential, the rotation matrix R_{IB} can be expressed as

$$R_{\mathrm{IB}} = e^{\tilde{e}_z\gamma} e^{\tilde{e}_y\beta} e^{\tilde{e}_x\alpha}. \tag{17}$$

For control purposes it will be convenient to obtain a linearization that is invariant to yaw. Therefore the position and velocity of the center of gravity will be expressed in a separate coordinate system $\{J\}$ obtained by rotating the inertial system $\{I\}$ about ${}_{\mathrm{I}}\vec{e}_z$ by the angle γ. Hence, the rotation matrix R_{IB} is decomposed according to

$$R_{\mathrm{IB}} = R_{\mathrm{IJ}} R_{\mathrm{JB}}, \quad R_{\mathrm{IJ}} = e^{\tilde{e}_z\gamma}, \quad R_{\mathrm{JB}} = e^{\tilde{e}_y\beta} e^{\tilde{e}_x\alpha}, \tag{18}$$

and (15) is reformulated as

$$m^{\mathrm{J}}\dot{v} = -m\dot{\gamma} e_z \times {}^{\mathrm{J}}v + m^{\mathrm{J}}g + R_{\mathrm{JB}} T_1 u, \tag{19}$$

where the convective derivative enters due to the fact that the frame $\{J\}$ is non-inertial. Linearizing the translational dynamics around hover, i.e. ${}^{\mathrm{J}}\bar{v} = 0,\ \bar{R}_{\mathrm{JB}} = I,\ \bar{\omega} = 0$, yields

$$\begin{aligned} {}^{\mathrm{J}}\dot{v} &\approx -\alpha\tilde{e}_x {}^{\mathrm{J}}g - \beta\tilde{e}_y {}^{\mathrm{J}}g + \frac{1}{m}T_1(u - \bar{u}) && (20) \\ &= g_0(\alpha\tilde{e}_x e_z + \beta\tilde{e}_y e_z) + \frac{1}{m}T_1(u - \bar{u}) && (21) \\ &= g_0(-e_y\alpha + e_x\beta) + \frac{1}{m}T_1(u - \bar{u}), && (22) \end{aligned}$$

which holds independent of the angle γ. Similarly, linearizing the rotational dynamics (16) around $\bar{\omega} = 0$, and neglecting the gyroscopic term $C\hat{\Theta}^{-1}\tilde{\omega}\omega_i$ results in

$$\dot{\omega} \approx \hat{\Theta}^{-1} T_2 u - \hat{\Theta}^{-1} e_z \sum_{i=1}^{3} M_i. \tag{23}$$

From (22) and (23) it can be inferred that the poles of the open-loop system all lie at 0, and that the height and yaw dynamics are decoupled from the x, y, and roll and pitch dynamics.

Assuming further that the mass distribution of the Flying Platform has a three-fold rotational symmetry about its figure axis ${}_{\mathrm{B}}\vec{e}_z$ simplifies the inertia tensor $\hat{\Theta}$ to

$$\hat{\Theta} =: \operatorname{diag}(I_1, I_1, I_3). \tag{24}$$

This is a reasonable assumption due to the symmetric placement of both the actuation units and the batteries, and the symmetry of the frame, which together constitute the main mass of the Flying Platform. Thus, the x, y, and roll and pitch dynamics can be rewritten as

$$\begin{pmatrix} \dot{v}_x \\ \dot{v}_y \end{pmatrix} \approx g_0 J \begin{pmatrix} \alpha \\ \beta \end{pmatrix} + \frac{1}{m}T_{11}(u - \bar{u}), \qquad \begin{pmatrix} \ddot{\alpha} \\ \ddot{\beta} \end{pmatrix} \approx \frac{1}{I_1}T_{21}(u - \bar{u}), \tag{25}$$

whereas the vertical and the yaw dynamics are given by

$$\dot{v}_z \approx \frac{1}{m} T_{12}(u - \bar{u}), \quad \ddot{\gamma} \approx \frac{1}{I_3} T_{22} u - \frac{1}{I_3} \sum_{i=1}^{3} M_i. \tag{26}$$

Controllability analysis. We determine the overall dimensions of the Flying Platform, that is the lengths l_1 and l_3 by maximizing the determinant of the controllability Gramian subject to the dynamics (25). This amounts to maximizing the volume of the state space from which the Flying Platform can be steered to zero within a fixed time T and with unit energy (assuming linear dynamics, i.e. near hover conditions), [26, Ch. 8]. We focus entirely on the actuation via thrust vectoring, and therefore the differential thrust is set to zero. As we will show in the remainder, this leads to a simple closed-form expression of the determinant of the controllability Gramian, which enables a physical interpretation, and leads to a straightforward optimization of the mechanical design.

By defining the state vector to be

$$x := (v_x, v_y, \alpha, \beta, \dot{\alpha}, \dot{\beta}), \tag{27}$$

the linearized system dynamics (25) can be rewritten in the standard form

$$\dot{x} = Ax + B(u - \bar{u}), \tag{28}$$

for which the controllability Gramian, [26, p. 227], is defined as

$$W_c(T) := \int_0^T e^{-At} B B^\top e^{-A^\top t} \mathrm{d}t. \tag{29}$$

The values of the matrices A and B are given in (A.1) in Appendix A. Given that we have unit energy at our disposal, the system can be steered within the time T to the origin from any initial condition within the ellipsoid

$$\mathcal{W}(T) := \{z \in \mathbb{R}^6 \mid z^\top W_c(T)^{-1} z \leq 1\}. \tag{30}$$

The area of $\mathcal{W}(T)$ is proportional to the square root of the determinant of $W_c(T)$. For the given dynamics, the determinant of $W_c(T)$ can be calculated in closed form, see Appendix A, leading to

$$\det(W_c(T)) = \frac{g_0^4 T^{18}}{102400} \left(\frac{l_3}{I_1}\right)^{12}. \tag{31}$$

The following observations can be made:

1) For any $I_1 \neq 0$, $l_3 \neq 0$ the Flying Platform can be steered from any initial condition to the origin, provided that T is sufficiently large. This is not surprising, as the system's poles all lie at 0.
2) The area of $\mathcal{W}(T)$ only depends on the inertia I_1 and the length l_3. The total mass, for example, enters the expression only through the inertia I_1.
3) For a fixed, but arbitrary T, the area of $\mathcal{W}(T)$ attains its maximum if the ratio l_3/I_1 is maximized.

Hence we chose the dimensions of the Flying Platform, l_1 and l_3, such that the ratio l_3/I_1 is as large as possible. Clearly, I_1 is implicitly dependent on l_3, as the actuation units have substantial mass. This dependence is captured by approximating the inertia I_1 as

$$I_1 \approx I_0 + 2(l_1^2 + l_3^2 \delta^2) m_t, \tag{32}$$

where m_t refers to the mass of a single actuation unit, whose center of gravity lies at a height of δl_3 below the center of gravity of the vehicle, and I_0 refers to the remaining inertia, which is independent of l_3. As a result, we seek to maximize the ratio

$$\frac{l_3}{I_0 + 2l_1^2 m_t + 2m_t \delta^2 l_3^2}, \tag{33}$$

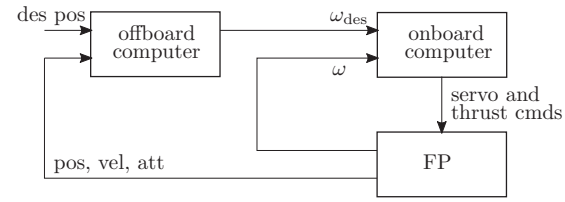

Fig. 11. Overview of the control architecture. FP stands for Flying Platform. The angular rates ω are measured with an onboard gyroscope. The position, velocity and attitude of the vehicle are obtained from a motion capture system.

which is achieved by decreasing I_0 and l_1 as much as possible. Moreover, for a fixed inertia I_0, length l_1, and mass m_t, the previous expression is maximized for

$$l_{3,\max} = \sqrt{\frac{\frac{I_0}{2m_t} + l_1^2}{\delta^2}}. \tag{34}$$

By assuming that the weight of the Flying Platform is mainly given by the actuation units and the weight of the batteries, which are located at a horizontal distance l_1 from the ${}_B\vec{e}_x$, respectively the ${}_B\vec{e}_y$ axis, we obtain $I_0 \approx 1.4$ kg l_1^2. Together with $m_t \approx 1.2$ kg, and $\delta \approx 0.75$ this yields $l_{3,\max} \approx 1.7 l_1$. In the design the length l_1 was bounded from below to $l_1 = 10$ cm for ease of assembly, and therefore l_3 was chosen to be roughly 17 cm.

The optimization over l_3 can be viewed as a trade-off between the total inertia of the flying vehicle and the lever arm of the thrust vectoring; the further away the actuation units are placed, the larger the lever arm, and the higher the torque generated by the thrust vectoring, but at the same time the inertia is increased. The lever arm grows linearly with l_3, whereas the inertia grows quadratically leading to the optimum captured by (34).

Moreover, the formula (31) is valid irrespective of the sign of l_3. Thus, the above derivation remains valid even in case the thrust vectoring is placed above the center of gravity. Note that having the thrust vectoring below the center of gravity leads to a non-minimum phase zero in the transfer function from the horizontal thrust to the horizontal velocity, as for example noted in [4]. It stems from the fact that the thrust vectoring generates lateral forces, which induce a torque with respect to the center of gravity, causing the vehicle to accelerate horizontally and tilt in the opposite direction at the same time. In case the thrust vectoring is placed above the center of gravity two complex conjugated, pure imaginary zeros are obtained instead. For ease of construction we decided to choose $l_3 > 0$.

4. Control design

We present a linear control design for stabilizing hover. The controller has a cascaded structure, with a part running onboard at 50 Hz, accessing onboard sensor measurements and controlling the angular rates of the vehicle, and a part running offboard, controlling the position and attitude, see Fig. 11.

Control system overview. The position, velocity, and attitude of the vehicle is estimated using a motion capture system, [27]. The system estimates position with a precision of roughly 0.3 mm, and attitude with a precision of roughly 0.3° (2σ-bounds, sampled at 200 Hz). The velocity is obtained by low-pass filtering and numerical differentiation of the position estimate. The data from the motion capture system is sent to an offboard computer, which implements a user interface and calculates the desired angular rates for the flying vehicle. The offboard computer runs at a sampling rate of 50 Hz. The desired angular rates are sent to the vehicle via a low-latency protocol, and are then tracked by the flying vehicle

using the gyroscope included on the PX4 flight computer. The onboard control algorithm runs at 50 Hz. Telemetry data from the flying vehicle is sent out via a separate wireless radio.

Onboard control. The onboard controller tracks the desired angular rates ω_{des}, which are obtained from the offboard computer. About hover, the rotational dynamics can be approximated by, c.f. (23),

$$\dot{\omega} = \hat{\Theta}^{-1} T_2 (u - \bar{u}), \tag{35}$$

where the torques M_i are approximated as constants, compensated by the steady-state control input $\bar{u}$. A linear quadratic regulator, with state weight $512 \cdot I$ and input weight

$$\text{diag}(\underbrace{1,2,2,}_{\substack{\text{1st actuation unit}\\ \text{x,y,z-components}}} \underbrace{1,2,2,}_{\substack{\text{2nd actuation unit}\\ \text{x,y,z-components}}} \underbrace{1,2,2}_{\substack{\text{3rd actuation unit}\\ \text{x,y,z-components}}}) \tag{36}$$

is used to compute a constant feedback gain K, rendering (35) asymptotically stable with

$$u = \bar{u} - K(\omega - \omega_{\text{des}}) + (0,0,1,0,0,1,0,0,1) F_z, \tag{37}$$

where F_z denotes the collective thrust of the three electric ducted fans. The collective thrust does not affect the angular rates and will be used in a later stage to control the height of the flying vehicle. The obtained feedback gain K results in closed-loop poles at 42 rad/s (for ω_x), 42 rad/s (for ω_y), and 25 rad/s (for ω_z).

Offboard control. Under the assumption that the inner control loop has a substantially faster time constant, we consider ω_{des} to be the control input of the outer control loop, controlling the position, attitude, and velocity of the flying vehicle. As a result, (22) simplifies to

$$\dot{v}_x \approx \beta g_0, \quad \dot{v}_y \approx -\alpha g_0, \quad \dot{v}_z = \frac{3}{m} F_z, \tag{38}$$

where ${}^J v =: (v_x, v_y, v_z)$. Differentiating the first two equations with respect to time yields

$$\ddot{v}_x = \omega_{\text{des},y} g_0, \quad \ddot{v}_y = -\omega_{\text{des},x} g_0. \tag{39}$$

Thus we choose

$$\omega_{\text{des},x} = \frac{1}{g_0}\big(-(2d_y w_y + p_y) g_0 \alpha + (w_y^2 + 2d_y w_y p_y) v_y + p_y w_y^2 (y - y_{\text{des}})\big), \tag{40}$$

$$\omega_{\text{des},y} = \frac{1}{g_0}\big(-(2d_x w_x + p_x) g_0 \beta - (w_x^2 + 2d_x w_x p_x) v_x - p_x w_x^2 (x - x_{\text{des}})\big), \tag{41}$$

$$\omega_{\text{des},z} = -\frac{1}{g_0} p_z (\gamma - \gamma_{\text{des}}), \tag{42}$$

$$F_z = \frac{m}{3}(-2d_z w_z v_z - w_z^2 (z - z_{\text{des}})), \tag{43}$$

where d_i, w_i, p_i with $i = x, y, z$ are constants, x, y, z and $x_{\text{des}}, y_{\text{des}}, z_{\text{des}}$ denotes the actual and desired position of the vehicle expressed in the $\{J\}$ frame, and γ_{des} the desired yaw angle. The constants d_i, w_i, p_i with $i = x, y$ are chosen such that the translational closed-loop dynamics in the $\{J\}$ frame result in two decoupled third-order systems with one pole located at $-p_x$ (respectively $-p_y$) and a remaining second-order system with damping d_x (respectively d_y) and natural frequency w_x (respectively w_y). The constant p_z determines the time-constant of the yaw dynamics, whereas the closed-loop dynamics for the height result in a second-order system with damping d_z and natural frequency w_z. The constants are set to the following values

Table 1
Root-mean-squared errors when hovering in steady state.

	rms error (x,y,z component)		
${}^I r$	0.013 m	0.029 m	0.005 m
ϕ	0.007°	0.004°	0.008°
ω	0.029 rad/s	0.022 rad/s	0.011 rad/s

$$d_x = d_y = d_z = 1,$$
$$\omega_x = \omega_y = 3\,\text{rad/s}, \quad \omega_z = 2\,\text{rad/s},$$
$$p_x = p_y = 1\,\text{rad/s}, \quad p_z = 2\,\text{rad/s},$$

leading to a clear separation of the time constants associated with the inner and the outer control loop. This results in a symmetric behavior in the x and y-directions, whereas the height is controlled in a slightly less aggressive manner ($\omega_z < \omega_x, \omega_y$). The damping is set to 1, leading to critically damped systems.

Flight experiments are carried out in the Flying Machine Arena, [27]. Table 1 shows the root-mean-squared errors when hovering in steady state. It follows that the vehicle maintains its position within a few centimeters. Disturbance rejection measurements are shown in Fig. 12. The disturbance is generated by commanding a constant angular rate in y-direction, $\omega_y = 0.3$ rad/s for 0.18 s, leading to a pitch of approximately 4° from which the vehicle is able to recover.

5. System identification

The following section describes a frequency domain-based approach for identifying the parameters of the Flying Platform. Specifically, the aim is to quantify the model quality and identify the matrices T_1/m and $\hat{\Theta}^{-1} T_2$, essentially determining the rotational and translational dynamics, (15) and (16). This is done by exciting the system while hovering with periodic, sinusoidal inputs, and measuring its reaction. Due to the fact that the system has nine inputs defined as the thrust commands of each actuation unit, at least nine different experiments are used to measure the corresponding frequency response function. In order to reduce the noise influence we performed in total 18 different experiments, which are based on two different excitation signals (for increasing robustness against nonlinearities, [28, Ch. 3]). The experiments, which are referred to by the subscript e, $e \in \{1, 2, \ldots, 18\}$, can be grouped in three parts: Part 1) ($e \in \{1, 4, 7, 10, 13, 16\}$): excitation of the control flaps 1 of each actuation unit; Part 2) ($e \in \{2, 5, 8, 11, 14, 17\}$): excitation of the control flaps 2 of each actuation unit; Part 3) ($e \in \{3, 6, 9, 12, 15, 18\}$): excitation of the vertical thrusts of each actuation unit. The different excitation signals are obtained by multiplying two scalar random phase multisine signals $S_1(j\omega)$ and $S_2(j\omega)$ (to be made precise below) with the 3-point discrete Fourier transform matrix $V(j\omega) \in \mathbb{C}^{3\times 3}$, resulting in

$$R(j\omega) = \begin{pmatrix} (V(j\omega) \otimes \text{diag}(\lambda)) S_1(j\omega) \\ (V(j\omega) \otimes \text{diag}(\lambda)) S_2(j\omega) \end{pmatrix}, \quad R(j\omega) \in \mathbb{C}^{18\times 9}, \tag{44}$$

where $\lambda \in \mathbb{R}^3, \lambda > 0$ represents a positive gain for scaling the excitation, and $\otimes$ refers to the Kronecker product. Multiplying the scalar multisine signals with the 3-point discrete Fourier transform matrix leads to an improved condition number of the pseudo-inverse needed to calculate the frequency response function, [28, p. 66]. The matrix $R(j\omega)$ contains the excitation signals for the different inputs as rows. Hence, for example in the first experiment of Part 1), the excitation signals $\lambda_1 V_{11}(j\omega) S_1(j\omega)$, $\lambda_1 V_{12}(j\omega) S_1(j\omega)$, $\lambda_1 V_{13}(j\omega) S_1(j\omega)$ are used to excite the control flaps 1 of each actuation unit (the remaining control flaps and the vertical thrusts are not excited). The multisine signals $S_1(j\omega)$ and $S_2(j\omega)$ have a random phase uniformly distributed in $[0, 2\pi)$, are sampled with 50 Hz,

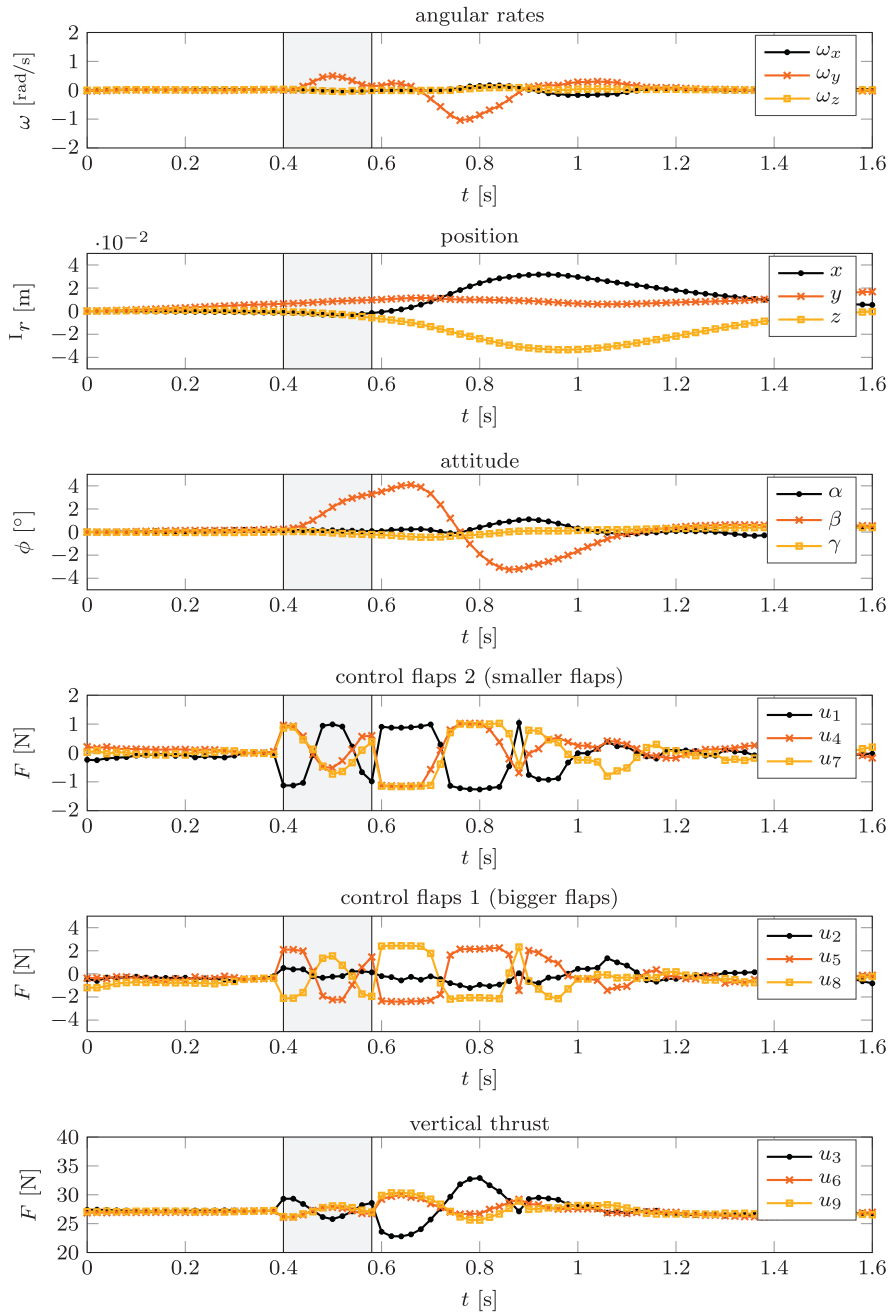

Fig. 12. Disturbance rejection. At time $t = 0.4$ s the disturbance is injected, by commanding angular rates of (0, 0.3 rad/s, 0) for 0.18 s. The time instances at which the disturbance is active are highlighted. The position and attitude (yaw) is shifted to zero at time 0.

and have a period of 250 samples. The Crest-factor, [28, p. 153] is reduced by optimizing over 1000 different phase-realizations. The resulting signal $S_1(j\omega)$ used for the identification is shown in Fig. 13, the signal $S_2(j\omega)$ has the same magnitude, but a different phase realization. Note that due to their periodicity, the random phase multisine signals prevent spectral leakage.

Thus, while hovering, the Flying Platform is excited with the signal $R_e(j\omega)$, where $R_e(j\omega)$ denotes the eth row of $R(j\omega)$. The setup is illustrated in Fig. 14. The periodic excitation leads naturally to a periodic input $U_e(j\omega)$ and a periodic output $Y_e(j\omega)$ (assuming the system is linear). The input is given by the thrust commands to each actuation unit, $u := ({}^1F_1, {}^2F_2, {}^3F_3)$ and the output is taken to be the angular velocity and the velocity of the center of mass, $y := ({}^{\mathrm{J}}v, \omega)$. By averaging over multiple periods the impact of the noise can be reduced, leading to

$$Y_e(j\omega) = \frac{1}{P}\sum_{p=1}^{P} Y_{ep}(j\omega), \quad Y_e(j\omega) \in \mathbb{C}^{12}, \tag{45}$$

$$U_e(j\omega) = \frac{1}{P}\sum_{p=1}^{P} U_{ep}(j\omega), \quad U_e(j\omega) \in \mathbb{C}^{9}, \tag{46}$$

where $P = 10$ refers to the number of periods, and $Y_{ep}(j\omega)$ refers to the Fourier transform of the output of the eth experiment and the pth period. In order to reduce the effect of transients the first 200 samples are discarded. In a similar way, the sample covariances are

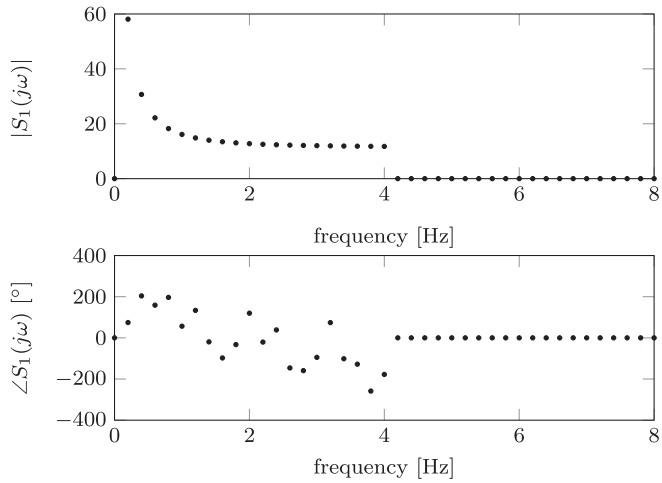

Fig. 13. Excitation signal $S_1(j\omega)$. The low frequencies have a larger magnitude to compensate the fact that the signal to noise ratio is worse at low frequencies. The excitation signal $S_2(j\omega)$ has the same magnitude, but a different phase realization.

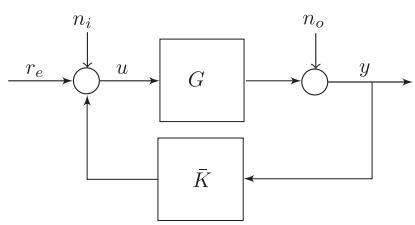

Fig. 14. The block diagram of the system identification procedure. The Flying Platform (G) is controlled by the nominal linear feedback controller $\bar{K}$, as presented in Section 4, and is excited by the random phase multisine signal r_e, that is, the time-domain representation of the signal $R_e(j\omega)$. The noise on the input and on the output is denoted by n_i, respectively n_0.

given by

$$\hat{\sigma}^2_{XZe}(j\omega) = \frac{1}{P(P-1)}\sum_{p=1}^{P} X_{ep}(j\omega) - X_e(j\omega)(Z_{ep}(j\omega) - Z_e(j\omega))^*, \tag{47}$$

where $X = U, Y,$ and $Z = U, Y$.

An estimate of the transfer function $G(j\omega)$ is obtained by combining the inputs and outputs of all experiments, i.e. $Y(j\omega) = (Y_1(j\omega), Y_2(j\omega), \ldots, Y_{18}(j\omega))$, $U(j\omega) = (U_1(j\omega), U_2(j\omega), \ldots, U_{18}(j\omega))$, and evaluating

$$G(j\omega) = Y(j\omega)U(j\omega)^\dagger, \tag{48}$$

where † denotes the pseudo-inverse. Due to the fact that the input and output noise is correlated, the pseudo-inverse leads to small biases in the estimate of $G(j\omega)$ (dependent on the signal to noise ratios). However, even for a moderate signal to noise ratio of 6dB these biases are on the order of few percents (relative to the true $G(j\omega)$), [28, p. 46].

The resulting transfer functions from the inputs to the angular velocity and the velocity of the center of mass are depicted in Fig. 15 and Fig. 16 (blue dots). The variance of the transfer function is estimated via

$$\begin{aligned}\hat{\sigma}^2_G(j\omega) = \frac{1}{E(E-1)}\sum_{e=1}^{E}(U_e(j\omega)U_e(j\omega)^*)^{-1} \otimes (\hat{\sigma}^2_{YYe}(j\omega) \\ -G(j\omega)\hat{\sigma}^2_{YUe}(j\omega)^* - \hat{\sigma}^2_{YUe}(j\omega)G(j\omega)^* \\ +G(j\omega)\hat{\sigma}^2_{UUe}(j\omega)G(j\omega)^*),\end{aligned} \tag{49}$$

where $E = 18$ refers to the number of experiments. Note that the variance $\hat{\sigma}_G(j\omega)$ has size 54×54 and refers to the variance of the vector $\mathrm{vec}(G(j\omega))$, where vec denotes vectorization.

5.1. Low-complexity model

We fit the parameters of the low-complexity model as derived in Section 3 to the measured frequency response. The parameters, denoted by θ, are given by the matrices T_1, T_2, and the inertia I_1 and I_3. We denote the parametric transfer function corresponding to the dynamics (25) by $G_\theta(j\omega)$. In addition, the parametric transfer function is augmented with a delay modeling the sample and hold. The parameters θ are obtained by optimizing the cost function

$$\begin{aligned}V(\theta) := \sum_{\omega\in\Omega} \mathrm{vec}(G_\theta(j\omega) - G(j\omega))^*(\hat{\sigma}^2_G(j\omega))^{-1} \\ \times \mathrm{vec}(G_\theta(j\omega) - G(j\omega)),\end{aligned} \tag{50}$$

where the set Ω is given by all frequencies that are excited by the excitation signal, that is, $\Omega := 2\pi\ \{0.2, 0.4, \ldots, 4\}$. Note that V is formed by the squared distance of the matrix elements of G_θ from G, weighted with the variance $\hat{\sigma}^2_G$. If $G_\theta(j\omega)$ is assumed to be circularly-symmetric complex normally distributed with variance $\hat{\sigma}^2_G(j\omega)$, then (50) corresponds to the maximum likelihood cost function.

The cost is optimized using a quasi-Newton method, where the Jacobian and Hessian are obtained via numerical differentiation. An absolute tolerance of 10^{-8} of the optimizer θ is used as a stopping criterion. The resulting fit is exemplarily shown for the angular velocity ω_x and the linear velocity v_y in Fig. 15, respectively Fig. 16. It can be concluded that the model explains well the frequencies above 1 Hz, but is not able to represent the lower frequencies accurately, which is most likely due to lack of aerodynamic effects in the model, as will be discussed in the following.

5.2. Augmented model

In order to explain the frequencies below 1 Hz the model is augmented to account for the following two effects, which were found to be dominant:

1) gyroscopic torques due to the fact that the ducted fans are all rotating in the same direction,
2) the redirection of a horizontal inlet airflow due to forward motion by the ducted fan leading to so-called momentum drag, [1].

According to (16), the gyroscopic torques are given by the term

$$-\tilde{\omega}\left(\Theta\omega + \sum_{i=1}^{3}\Theta_i\omega_i\right), \tag{51}$$

whose linearization about hover yields

$$3C\omega_{T_0}\tilde{e}_z\omega, \tag{52}$$

with ω_{T_0} the angular velocity of a single ducted fan at hover.

The second effect stems from the fact that the airflow is redirected by the electric ducted fan and the outlet nozzle, leading to drag-like forces acting on the Flying Platform, see Fig. 17. This force is modeled to be proportional to the velocity at a certain point P_i (to be determined by the measured data), [5],

$$F_{M_i} = -C_\alpha(v + \omega \times r_{Pi}), \quad i = 1, 2, 3, \tag{53}$$

$$C_\alpha := \mathrm{diag}(c_{\alpha_1}, c_{\alpha_1}, c_{\alpha_2}), \tag{54}$$

where r_{Pi} denotes the vector from the center of gravity to the point P_i and $c_{\alpha_1} > 0$, $c_{\alpha_2} > 0$ are two constants. The different constants

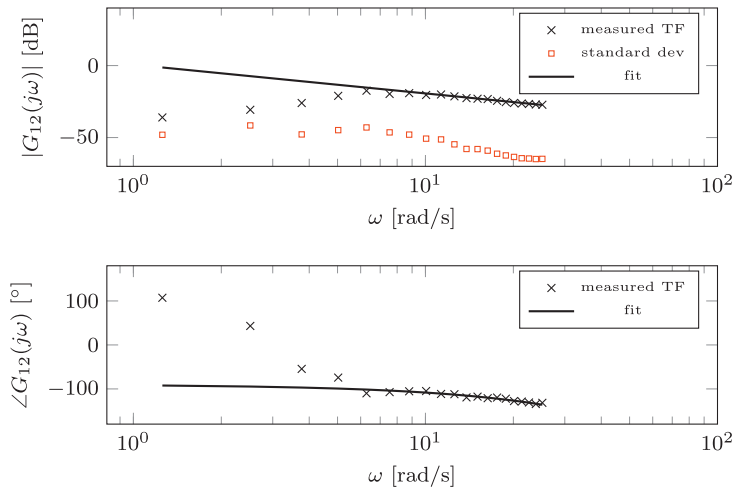

Fig. 15. Estimated transfer function (black crosses) from the control flap 1 (bigger flap) of the first actuation unit to the angular rates ω_x. The resulting fit of the simplified model is shown in black (solid line) and the estimate of the standard deviation is depicted in red (squares). (For interpretation of the references to color in this figure legend, the reader is referred to the web version of this article.)

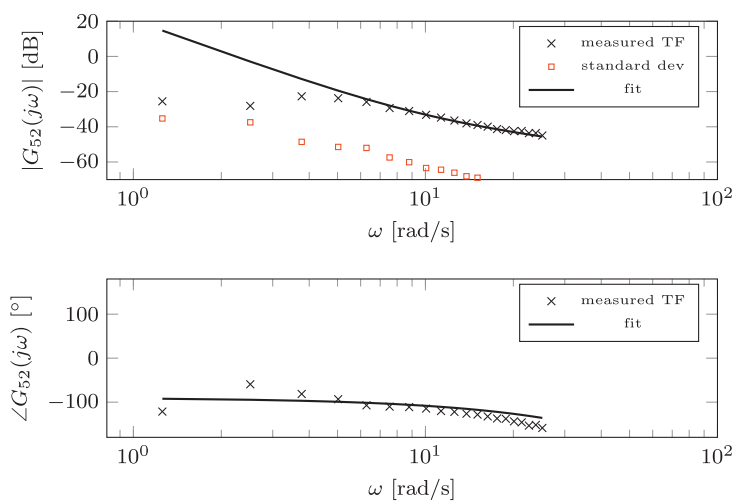

Fig. 16. Estimated transfer function (black crosses) from the control flap 1 (bigger flap) of the first actuation unit to the velocity v_y. The resulting fit of the simplified model is shown in black (solid line) and the estimate of the standard deviation is depicted in red (squares). (For interpretation of the references to color in this figure legend, the reader is referred to the web version of this article.)

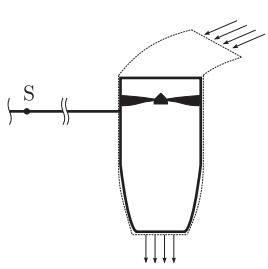

Fig. 17. A single actuation unit with a body-fixed control volume (dashed line). The arrows refer to the inlet, respectively the outlet flow. An incoming airflow having a lateral component, which might stem from a translational motion is redirected by the electric ducted fan and the outlet nozzle, leading to a drag-like force acting on the Flying Platform (as can be seen from a momentum balance over the control volume).

c_{α_1} and c_{α_2} aim at modeling a potentially different behavior for horizontal and vertical motions. In addition, these forces induce a torque with respect to the center of gravity. As a result, due to the three-fold rotational symmetry of the fan configuration, the total force is modeled as

$$F_M := \sum_{i=1}^{3} F_{M_i} = -3C_\alpha v + 3l_{\alpha_1} C_\alpha \tilde{e}_z \omega, \tag{55}$$

and the total torque (with respect to the center of gravity) is modeled as

$$M_M := -3l_{\alpha_2} C_\alpha \tilde{e}_z v - 3L_\alpha C_\alpha \omega, \tag{56}$$

where

$$L_\alpha := \mathrm{diag}(l_{\alpha_3}, l_{\alpha_3}, l_{\alpha_4}), \tag{57}$$

and c_α, l_{α_1}, l_{α_2}, l_{α_3}, and l_{α_4} refer to different lengths describing the points P_i and the lever arms of the forces F_{M_i}. Note that the constants c_{α_1} and c_{α_2} have units Ns/m, l_{α_1} and l_{α_2} have units m, and l_{α_3} and l_{α_4} have units m^2.

Combining these three effects yields the augmented linear model

$$\dot{x}_a = A_a x_a + B_a(u - \bar{u}), \tag{58}$$

where $x_a := ({}^{\mathrm{J}}v, \alpha, \beta, \gamma, \omega)$, and

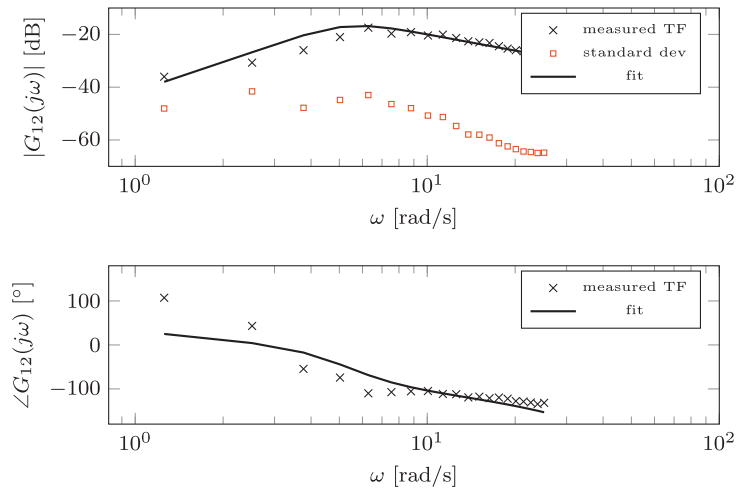

Fig. 18. Estimated transfer function (black crosses) from the control flap 1 (larger flap) of actuation unit 1 to the angular rate ω_x. The fit resulting from the augmented model is shown in black (solid line) and the standard deviation is indicated in red (squares). (For interpretation of the references to color in this figure legend, the reader is referred to the web version of this article.)

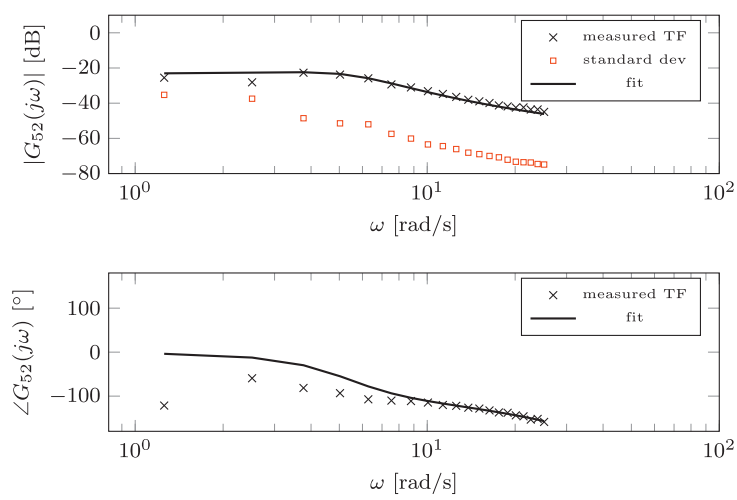

Fig. 19. Estimated transfer function (black crosses) from the control flap 1 (larger flap) of actuation unit 1 to the velocity v_y. The fit resulting from the augmented model is shown in black (solid line) and the standard deviation is indicated in red (squares). (For interpretation of the references to color in this figure legend, the reader is referred to the web version of this article.)

$$A_a := \begin{pmatrix} -3\frac{c_{\alpha_1}}{m} & 0 & 0 & 0 & g_0 & 0 & 0 & -3\frac{l_{\alpha_1}c_{\alpha_1}}{m} & 0 \\ 0 & -3\frac{c_{\alpha_1}}{m} & 0 & -g_0 & 0 & 0 & 3\frac{l_{\alpha_1}c_{\alpha_1}}{m} & 0 & 0 \\ 0 & 0 & -3\frac{c_{\alpha_2}}{m} & 0 & 0 & 0 & 0 & 0 & 0 \\ 0 & 0 & 0 & 0 & 0 & 0 & 1 & 0 & 0 \\ 0 & 0 & 0 & 0 & 0 & 0 & 0 & 1 & 0 \\ 0 & 0 & 0 & 0 & 0 & 0 & 0 & 0 & 1 \\ 0 & 3\frac{l_{\alpha_2}c_{\alpha_1}}{I_1} & 0 & 0 & 0 & 0 & -3\frac{l_{\alpha_3}c_{\alpha_1}}{I_1} & -3\frac{C\omega_{T_0}}{I_1} & 0 \\ -3\frac{l_{\alpha_2}c_{\alpha_1}}{I_1} & 0 & 0 & 0 & 0 & 0 & 3\frac{C\omega_{T_0}}{I_1} & -3\frac{l_{\alpha_3}c_{\alpha_1}}{I_1} & 0 \\ 0 & 0 & 0 & 0 & 0 & 0 & 0 & 0 & -3\frac{l_{\alpha_4}c_{\alpha_2}}{I_3} \end{pmatrix}, \quad B_a := \begin{pmatrix} \frac{1}{m}T_{11} \\ \frac{1}{m}T_{12} \\ 0_{3\times 9} \\ \frac{1}{I_1}(I_3 J T_{11} + 2\sqrt{3}/3 I_1 V_1) \\ \frac{1}{I_3}T_{22} \end{pmatrix}.$$

The parameters θ_a, describing the augmented parametric transfer function are given by $c_{\alpha_1}, c_{\alpha_2}, l_{\alpha_1}, l_{\alpha_2}, l_{\alpha_3}, l_{\alpha_4}, T_1, T_2, V_1$, and are found by optimizing (50) (with respect to the augmented model). The remaining parameters m, l_1, and I_1 are fixed to $m = 8$ kg, $l_1 = 10$ cm, and $I_1 = 0.07$ kg m^2 (a rough estimate from the CAD-model) to eliminate redundancies, and a delay accounting for the sample-and-hold is included. The resulting fit is exemplarily shown for the angular velocity ω_x and the linear velocity v_y in Figs. 18 and 19. Compared to the low-complexity model, the augmented model captures the behavior at frequencies below 1 Hz substantially better. By introducing the augmented model, the cost function $V(\theta)$ is decreased by roughly two orders of magnitude, which corresponds to a reduction of 99%. Most of the decrease can be attributed to introduction of the momentum drag, as the introduction of the gyroscopic effects leads to a decrease of the cost of roughly 1.3%.

We further investigated the sensitivity of the cost function with respect to shifts in the center of gravity, variations of the iner-

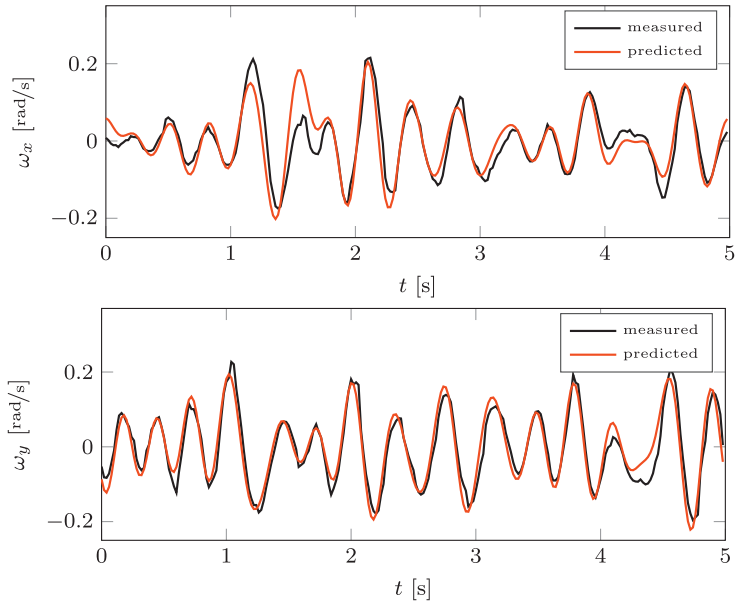

Fig. 20. Validation of the augmented model. The Flying Platform is excited by a random phase multisine signal acting on the control flaps 1. The measurements are averaged over 8 periods to reduce the noise influence. The estimated standard deviation of the measurements is on the order of few percent and is therefore not shown.

Table 2
Sensitivity of the cost function $V(\theta)$ estimated from monte-carlo sampling. The parameter variations, that is, a shift in the center of gravity (COG shift), variations in the inertia (inertia), and a misalignment of coordinate systems (misalignment) are uniformly sampled, and the corresponding variation of the cost is quantified by the ratio between its standard deviation and its expected value. The shift in the center of gravity is restricted to a radius of 2 cm and the variations of the inertia are obtained by varying the diagonal elements of diag(I_1, I_1, I_3) by 5% and rotating the resulting matrix along a uniformly sampled direction by an angle of less than 2° (also uniformly sampled). The misalignment of coordinate systems is characterized by rotations comprising a uniformly sampled direction and a uniformly sampled rotation angle of less than 2°.

parameter var.	std[$V(\theta)$]/E[$V(\theta)$]	Number samples
COG shift	0.027	10^4
Inertia	0.0045	10^5
Misalignment	0.0085	10^5
All	0.029	10^7

tia, and misalignment of coordinate systems used for measuring ${}^{J}v$ and ω. To that extent, we analyzed the standard deviation of the cost function when sampling these parameter variations uniformly. The results are reported in Table 2. The cost is most sensitive to shifts in the center of gravity. However, even in case all effects are included, the cost alters by less than 3%, which is small especially when considering the number of additional degrees of freedom that these variations introduce. Thus, although a higher-order model might explain the data even better, we believe that the augmented model we presented yields a reasonable trade-off between model complexity and accuracy. The resulting numerical parameter values are listed in Appendix B. The full fit of the augmented model to the experimental data can be found on the first author's homepage.[7]

[7] http://www.idsc.ethz.ch/research-dandrea/people/person-detail.html?persid=156097.

We validated the model on a different dataset. The resulting time-domain fit of the angular velocities ω_x and ω_y is exemplarily depicted in Fig. 20.

6. Conclusion

This article presented the mechatronic design of the Flying Platform, an aerial vehicle whose purpose is to study ducted fan actuation. We discussed the mechanical design of a single actuation unit, including the control flap design to vector the thrust. The resulting thrust vectoring capabilities were characterized by static and dynamic measurements. A low-complexity rigid body model was introduced for control and analysis purposes. In particular, it was shown that the determinant of the controllability Gramian is a function of the ratio between lever arm and inertia. As a result, the mechanical design of the Flying Platform was chosen to maximize controllability. A linear control design was presented subsequently, which was shown to work reliably in practice. The quality of the model was assessed via a frequency domain system identification. It was shown that the low-complexity model captures roughly the frequencies above 1 Hz, but is unable to explain the lower frequencies. As a result, the model was extended to incorporate gyroscopic and aerodynamic effects, while keeping the model order fixed. The augmented model was found to roughly explain the measured transfer function from vectored thrusts to angular and linear velocities even at frequencies below 1 Hz.

It is hoped that the modeling and the measurement results presented throughout this article are useful for future aerial vehicle designs, and/or feasibility studies of aerial vehicles propelled by ducted fans.

Possible future work includes performing more aggressive maneuvers and evaluating advanced control algorithms, that account, for example, for input and state constraints, or incorporate the nonlinearities in the attitude dynamics. The ducted fan actuation, as presented in this paper, could be used for controlling aerial vehicles with lifting surfaces, thereby enabling efficient forward flight combined with high maneuverability, and vertical take-off and landing capabilities.

Acknowledgment

This research was supported by the ETH-Grant ETH-48 15-1. We would like to thank Tobias Meier and Yeo Yih Tang for numerous contributions, for example to the flap design, the characterization of a single actuation unit, and the implementation of low-level hardware interfaces. We would like to express our gratitude towards Michael Egli and Marc-Andrè Corzillius for their contribution to the mechanical and electrical design. We would like to thank the Flying Machine Arena members for sharing the software and hardware infrastructure. A list of past and present participants is available at http://flyingmachinearena.org/people/.

Appendix A. Determinant of controllability Gramian

The system matrices in (28) are given by

$$A := \begin{pmatrix} 0 & g_0 J & 0 \\ 0 & 0 & I \\ 0 & 0 & 0 \end{pmatrix}, \quad B := \begin{pmatrix} \frac{1}{m} T_{11} \\ 0 \\ \frac{l_3}{I_1} J T_{11} \end{pmatrix}. \tag{A.1}$$

The matrix exponential e^{-At} yields therefore

$$e^{-At} = \begin{pmatrix} I & -g_0 t J & \frac{g_0 t^2}{2} J \\ 0 & I & -tI \\ 0 & 0 & I \end{pmatrix}, \tag{A.2}$$

leading to

$$e^{-At} B = \frac{l_3}{I_1} \begin{pmatrix} (\frac{I_1}{l_3 m} - \frac{g_0 t^2}{2}) T_{11} \\ -tJT_{11} \\ JT_{11} \end{pmatrix}, \tag{A.3}$$

and

$$e^{-At} B B^{\mathsf{T}} e^{-At} = \left(\frac{l_3}{I_1}\right)^2 \operatorname{diag}(I,J,J) \begin{pmatrix} \zeta^2 & -\zeta t & \zeta \\ -\zeta t & t^2 & -t \\ \zeta & -t & 1 \end{pmatrix} \otimes T_{11} T_{11}^{\mathsf{T}} \operatorname{diag}(I,J,J)^{\mathsf{T}}, \tag{A.4}$$

where $\zeta := I_1/(l_3 m) - g_0 t^2/2$. This yields

$$\det(W_c(T)) = \left(\frac{l_3}{I_1}\right)^{12} \det\left(\int_0^T \begin{pmatrix} \zeta^2 & -\zeta t & \zeta \\ -\zeta t & t^2 & -t \\ \zeta & -t & 1 \end{pmatrix} \mathrm{d}t\right)^2 \det(T_{11} T_{11}^{\mathsf{T}})^3, \tag{A.5}$$

where the fact that $\det(\operatorname{diag}(I,J,J)) = 1$ and the property $\det(X \otimes Y) = \det(X)^m \det(Y)^n$ of the Kronecker product has been used (where $X \in \mathbb{R}^{n\times n}$ and $Y \in \mathbb{R}^{m\times m}$). Moreover, $T_{11} T_{11}^{\mathsf{T}}$ simplifies to $3I$, and therefore, we obtain

$$\det(W_c(T)) = 9^3 \left(\frac{l_3}{I_1}\right)^{12} \det\left(\int_0^T \begin{pmatrix} \zeta^2 & -\zeta t & \zeta \\ -\zeta t & t^2 & -t \\ \zeta & -t & 1 \end{pmatrix} \mathrm{d}t\right)^2. \tag{A.6}$$

Using straightforward manipulations it can be shown that

$$\det\left(\int_0^T \begin{pmatrix} \zeta^2 & -\zeta t & \zeta \\ -\zeta t & t^2 & -t \\ \zeta & -t & 1 \end{pmatrix} \mathrm{d}t\right) = \frac{g_0^2}{8640} T^9, \tag{A.7}$$

which results in

$$\det(W_c(T)) = \frac{g_0^4 T^{18}}{102400} \left(\frac{l_3}{I_1}\right)^{12}. \tag{A.8}$$

Table B.3
Scalar parameters of the augmented model. Note that the values of I_1 and I_3 are estimated using a CAD model. The value of C is obtained by dividing $C\omega_{T_0}$ by a rough estimate of the fan velocity at hover (obtained from the datasheet of the manufacturer of the ducted fan).

	Value	Comment
m	8 kg	Mass
l_1	0.1 m	Lever arm of actuation
l_3	0.079 m	Lever arm of actuation
I_1	0.07 kg m^2	Inertia (roll, pitch, estimate)
I_3	0.11 kg m^2	Inertia (yaw)
C	$7 \cdot 10^{-6}$ kg m^2	Inertia of moving parts (motor and fan)
c_{α_1}	2.388 Ns/m	Drag force
c_{α_2}	4.939 Ns/m	
l_{α_1}	0.242 m	
l_{α_2}	−0.138 m	Drag force - lever arm
l_{α_3}	−0.0084 m^2	
l_{α_4}/I_3	0.362 kg^{-1}	
$C\omega_{T_0}$	0.018 kg m^2/s	Gyroscopic effects
T_d	0.045 s	Time delay

Appendix B. Parameter values

The parameter values of the augmented model are listed below. The matrices T_1 and T_2 are given by

$$T_{11} = \begin{pmatrix} 0.6966 & -0.0311 & 0 & -0.3643 & -0.7165 & 0 & -0.3867 & 0.7286 & 0 \\ 0.0330 & 0.8656 & 0 & 0.6447 & -0.3826 & 0 & -0.6196 & -0.3775 & 0 \end{pmatrix},$$

$$T_{12} = \begin{pmatrix} 0 & 0 & 0.0967 & 0 & 0 & 0.0896 & 0 & 0 & 0.0670 \end{pmatrix},$$

$$V_1 = \begin{pmatrix} 0 & 0 & 0.0156 & 0 & 0 & -0.3433 & 0 & 0 & 0.3873 \\ 0 & 0 & 0.4450 & 0 & 0 & -0.2501 & 0 & 0 & -0.2068 \end{pmatrix},$$

$$\frac{1}{I_3} T_{22} = \begin{pmatrix} 0 & -0.7062 & -0.1536 & 0 & -0.6859 & -0.1030 & 0 & -0.7037 & -0.1076 \end{pmatrix}.$$

This leads to the following system matrices

$$A_a = \begin{pmatrix} -0.896 & 0 & 0 & 0 & 9.810 & 0 & 0 & -0.217 & 0 \\ 0 & -0.896 & 0 & -9.810 & 0 & 0 & 0.217 & 0 & 0 \\ 0 & 0 & -1.852 & 0 & 0 & 0 & 0 & 0 & 0 \\ 0 & 0 & 0 & 0 & 0 & 0 & 1 & 0 & 0 \\ 0 & 0 & 0 & 0 & 0 & 0 & 0 & 1 & 0 \\ 0 & 0 & 0 & 0 & 0 & 0 & 0 & 0 & 1 \\ 0 & -14.136 & 0 & 0 & 0 & 0 & 0.856 & -0.751 & 0 \\ 14.136 & 0 & 0 & 0 & 0 & 0 & 0.751 & 0.856 & 0 \\ 0 & 0 & 0 & 0 & 0 & 0 & 0 & 0 & -5.366 \end{pmatrix}, \tag{B.1}$$

$$B_a = \begin{pmatrix} 0.087 & -0.004 & 0 & -0.046 & -0.090 & 0 & -0.048 & 0.091 & 0 \\ 0.004 & 0.108 & 0 & 0.081 & -0.048 & 0 & -0.077 & -0.047 & 0 \\ 0 & 0 & 0.097 & 0 & 0 & 0.090 & 0 & 0 & 0.067 \\ 0 & 0 & 0 & 0 & 0 & 0 & 0 & 0 & 0 \\ 0 & 0 & 0 & 0 & 0 & 0 & 0 & 0 & 0 \\ 0 & 0 & 0 & 0 & 0 & 0 & 0 & 0 & 0 \\ 0.037 & 0.980 & 0.026 & 0.730 & -0.433 & -0.566 & -0.702 & -0.427 & 0.639 \\ -0.789 & 0.035 & 0.734 & 0.413 & 0.811 & -0.413 & 0.438 & -0.825 & -0.341 \\ 0 & -0.706 & -0.154 & 0 & -0.686 & -0.103 & 0 & -0.704 & -0.108 \end{pmatrix}. \tag{B.2}$$

References

[1] Robson G, D'Andrea R. Longitudinal stability of a jet-powered wingsuit. In: Proceedings of the AIAA Guidance, Navigation, and Control Conference; 2010.
[2] Leishman JG. Principles of helicopter aerodynamics. Second ed. Cambridge University Press; 2006.
[3] Johnson EN, Turbe MA. Modeling, control, and flight testing of a small ducted-fan aircraft. J. Guidance Contr. Dyn. 2006;29(4):769–79.
[4] Marconi L, Naldi R. Control of aerial robots. Contr. Syst. Mag. 2012;32:43–65.
[5] Pflimlin J-M, Binetti P, Souères P, Hamel T, Trouchet D. Modeling and attitude control analysis of a ducted-fan micro aerial vehicle. Control. Eng. Pract. 2010;18(3):209–18.
[6] Pflimlin JM, Souères P, Hamel T. Hovering flight stabilization in wind gusts for ducted fan UAV. In: Proceedings of the 43rd Conference on Decision on Control; 2004. p. 3491–6.
[7] Olfati-Saber R. Global configuration stabilization for the VTOL aircraft with strong input coupling. IEEE Trans. Automat. Contr. 2002;47(11):1949–52.
[8] Hess RA, Bakhtiari-Nejad M. Sliding mode control of a nonlinear ducted-fan UAV model. In: Proceedings of the AIAA Guidance, Navigation, and Control Conference; 2006. p. 748–62.

[9] Franz R, Milam M, Hauser J. Applied receding horizon control of the caltech ducted fan. In: Proceedings of the American Control Conference; 2002. p. 3735–40.
[10] Peddle IK, Jones T, Treurnicht J. Practical near hover flight control of a ducted fan (SLADe). Control Eng. Pract. 2009;17(1):48–58.
[11] Fleming J, Jones T, Ng W, Gelhausen P, Enns D. Improving control system effectiveness for ducted fan VTOL UAVs operating in crosswinds. In: Proceedings of the 2nd AIAA "Unmanned Unlimited" System, Technologies and Operations-Aerospace Conference; 2003.
[12] Pereira JL. Hover and Wind-Tunnel Testing of Shrouded Rotors for Improved Micro Air Vehicle Design. Ph.D. thesis. University of Maryland; 2008.
[13] Akturk A, Camci C. Experimental and computational assessment of a ducted–fan rotor flow model. J. Aircr. 2012;49(3):885–97.
[14] Hrishikeshavan V, Black J, Chopra I. Development of a quad shrouded rotor mircro air vehicle and performance evaluation in edgewise flow. In: Proceedings of the American Helicopter Society Forum; 2012.
[15] Miwa M, Uemura S, Ishihara Y, Imamura A, hwan Shim J, Ioi K. Evaluation of quad ducted-fan helicopter. Int. J. Intell. Unmanned Syst. 2013;1(2):187–98.
[16] Imamura A, Miwa M, Hino J. Flight characteristics of quad rotor helicopter with thrust vectoring equipment. J. Rob. Mech. 2016;28(3):334–42.
[17] Hamel PG, Jategaonkar RV. Evolution of flight vehicle system identification. J. Aircr. 1996;33(1):9–28.
[18] Mettler B, Tischler MB, Kanade T. System identification of small-size unmanned helicopter dynamics. In: Proceedings of the American Helicopter Society Forum; 1999.
[19] Dorobantu A, Murch AM, Mettler B, Balas GJ. Frequency domain system identification for a small, low-cost, fixed-wing UAV. In: Proceedings of the AIAA Guidance, Navigation, and Control Conference; 2011.
[20] Derafa L, Madani T, Benallegue A. Dynamic modelling and experimental identification of four rotors helicopter parameters. In: Proceedings of the International Conference on Industrial Technology; 2006. p. 1834–9.
[21] Hoffer NV, Coopmans C, Jensen AM, Chen Y. A survey and categorization of small low-cost unmanned aerial vehicle system identification. J. Intell. Rob. Syst. 2014;74(1):129–45.
[22] Lewis KW. The Cumulative Effects of Roughness and Reynolds Number on NACA 0015 Airfoil Section Characteristics. Texas Tech University; 1984. Master's thesis in Mechanical Engineering.
[23] Freudenreich K, Kaiser K, Schaffarczyk A, Winkler H, Stahl B. Reynolds number and roughness effects on thick airfoils for wind turbines. Wind Eng. 2004;28(5):529–46.
[24] PX4 flight management unit. https://pixhawk.org/modules/px4fmu; Accessed: July 2016.
[25] Pfeiffer F, Glocker C. Multibody Dynamics with Unilateral Contacts. Wiley-VCH; 2004.
[26] Callier FM, Desoer CA. Linear System Theory. Springer Science + Business Media; 1991.
[27] Lupashin S, Hehn M, Mueller MW, Schoellig AP, Sherback M, D'Andrea R. A platform for aerial robotics research and demonstration: the flying machine arena. Mechatronics 2014;24:41–54.
[28] Pintelon R, Schoukens J. System Identification: A Frequency Domain Approach. Second ed. John Wiley & Sons; 2012.

Michael Muehlebach received the B.Sc. and M.Sc. degrees from ETH Zurich in 2010 and 2013, respectively. He received the Outstanding D-MAVT Bachelor Award and was awarded the Willi-Studer prize for the best Master's degree in Robotics, Systems, and Control. He did his Master's thesis on variational integrators for Hamiltonian systems and their application to multibody dynamics. He is currently a PhD student at ETH Zurich in the Institute for Dynamic Systems and Control. His main interests include multibody dynamics, the control of nonlinear systems, and model predictive control.

Raffaello D'Andrea received the B.Sc. degree in Engineering Science from the University of Toronto in 1991, and the M.S. and Ph.D. degrees in Electrical Engineering from the California Institute of Technology in 1992 and 1997. He was an assistant, and then an associate, professor at Cornell University from 1997 to 2007. While on leave from Cornell, from 2003 to 2007, he co-founded Kiva Systems, where he led the systems architecture, robot design, robot navigation and coordination, and control algorithms efforts. He is currently professor of Dynamic Systems and Control at ETH Zurich, and chairman of the board at Verity Studios AG.